Supporting Information for:

The Environment-Dependent Behavior of the Blatter Radical at the Metal-Molecule Interface

Jonathan Z. Low[a,⊥], Gregor Kladnik[b,c,⊥], Laerte L. Patera[d], Sophia Sokolov[d], Giacomo Lovat[e], Elango Kumarasamy[a], Jascha Repp[d], Luis M. Campos*[,a], Dean Cvetko*[,b,c,f], Alberto Morgante*[,c,g], Latha Venkataraman*[,a,e]

[a]Department of Chemistry, Columbia University, New York, New York 10027, United States

[b]Faculty of Mathematics and Physics, University of Ljubljana, 1000 Ljubljana, Slovenia

[c]CNR-IOM Laboratorio Nazionale TASC, Basovizza, SS-14, km 163.5, I-34012 Trieste, Italy

[d]Institute of Experimental and Applied Physics, University of Regensburg, 93053 Regensburg, Germany

[e]Department of Applied Physics and Applied Mathematics, Columbia University, New York, New York 10027, United States

[f]J. Stefan Institute, Jamova 39, SI-1000 Ljubljana, Slovenia

[g]Department of Physics, University of Trieste, 34127 Trieste, Italy

[⊥]Both authors contributed equally to this work.

Contents

1. General experimental – NMR, mass spectrometry, UV-Vis spectrometry, EPR

^{1}H-NMR and ^{13}C-NMR were performed using a Bruker Avance III 400 (400 MHz) or Avance III 500 (500 MHz) NMR spectrometer. Mass spectra were recorded on a XEVO G2-XS Waters® Mass Spectrometer with a QTOF detector at the Columbia University Mass Spec Facility. Either electrospray ionization (ESI), atmospheric pressure chemical ionization (APCI), or atmospheric solids analysis probe (ASAP) were used for ionization as indicated. Absorption spectra were recorded on a Shimadzu UV 1800 UV-Vis spectrophotometer. X-band Electron paramagnetic resonance (EPR) spectra were recorded on a Bruker EMX spectrometer using a modulation amplitude of 0.50 G. The sample was dissolved in toluene and placed in quartz tubes with 4 mm inner diameter. Argon was bubbled through the solution prior to sealing the tube.

2. Synthetic details

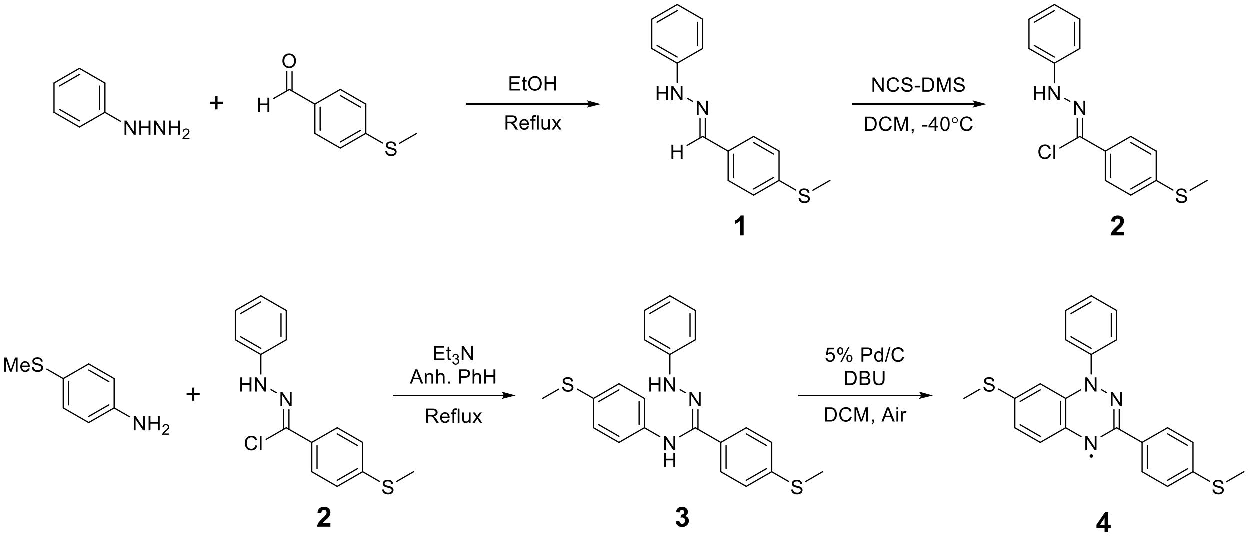

Scheme S1. Synthesis of the Blatter radical derivative.

***Compound 1** – prepared according to a reported method with different starting reagents*[1]

Phenylhydrazine (9.4g, 87.4mmol, 1eq) was dissolved in ethanol (200mL). 4-(methylthio)benzaldehyde (13.3g, 87.4mmol, 1eq) was slowly added with stirring. A precipitate formed almost immediately. The solution was refluxed for a further 5h, then cooled to room temperature. The precipitate was collected and recrystallized from ethanol to yield the desired hydrazone **1** as an off-white solid (17.1g, 81%). ^{1}H-NMR (400 MHz, CD_2Cl_2) δ 7.66 (s, 1H), 7.59 (d, J = 8.4 Hz, 2H), 7.30 – 7.22 (m, 4H), 7.11 (d, J = 7.6 Hz, 2H), 6.86 (t, J = 7.6 Hz, 1H), 2.51 (s, 3H). ^{13}C-NMR (500 MHz, CD_2Cl_2) δ 144.80, 139.17, 136.93, 132.22, 129.25, 126.44, 126.18, 119.93, 112.54, 15.31. HRMS (ASAP+) Calculated $[M+H]^+$ 243.0956, observed 243.0954.

***Compound 2** – prepared according to a reported method with different starting reagents*[2]

This hydrazonyl chloride was prepared via a reported procedure using the Corey-Kim reagent (NCS-DMS). *N*-chlorosuccinimide (2.15g, 16.1mmol, 1.3eq) was dissolved in dry DCM (160mL) under an inert atmosphere and cooled to 0°C. Dimethyl sulfide (1.16g, 18.6mmol, 1.5eq) was added to the stirring solution, which was then stirred for a further 5 min at 0°C. The solution was cooled to -40°C, and the hydrazone **1** (3.0g, 12.4mmol, 1eq) was added as a solid. The solution was stirred at -40°C for 1.5h and allowed to warm to 0°C over 1h. The reaction was quenched with cold water and extracted twice with DCM. The organic extracts were washed with water and brine and dried over $MgSO_4$. The solvent was removed, and the crude product was purified by column chromatography (silica gel, 20% DCM in hexanes) to yield the product as an off-white solid (1.86g, 54%). ^{1}H-NMR (400 MHz, CD_2Cl_2) δ 8.06 (s, 1H), 7.85 (d, *J* = 8.8 Hz, 2H), 7.34 – 7.25 (m, 4H), 7.21 – 7.16 (m, 2H), 6.94 (t, *J* = 7.6 Hz, 1H), 2.52 (s, 3H). ^{13}C-NMR (500 MHz, CD_2Cl_2) δ 143.46, 140.66, 130.97, 129.34, 126.58, 125.60, 124.40, 121.05, 113.29, 15.08. HRMS (ASAP+) Calculated $[M+H]^+$ 277.0566, observed 277.0560.

***Compound 3** – prepared according to a reported method with different starting reagents*[3]

The hydrazonyl chloride **2** (1.80g, 6.50mmol, 1eq) and 4-(methylthio)aniline (0.91g, 6.50mmol, 1eq) were dissolved in dry benzene (20mL) under an inert atmosphere. Triethylamine (0.99g, 9.76mmol, 1.5eq) was added, and the solution was refluxed for 3-4h. The reaction was quenched with cold water and diluted with ethyl acetate. The organic extracts were washed with water and brine and dried over $MgSO_4$. After removing the solvent, the crude product was purified by column chromatography (silica gel, 10-20% ethyl acetate in hexanes) to yield the amidrazone as an off-white solid (0.81g, 33%). ^{1}H-NMR (400 MHz, CD_2Cl_2) δ 7.65 – 7.59 (m, 3H), 7.28 – 7.15 (m, 6H), 7.13 – 7.07 (m, 2H), 6.85 (t, *J* = 7.6 Hz, 1H), 6.67 (d, *J* = 8.4 Hz, 2H), 5.72 (s, 1H), 2.49 (s, 3H), 2.42 (s, 3H). ^{13}C-NMR (500 MHz, $CDCl_3$) δ 145.14, 139.80, 139.77, 137.89, 131.12, 129.59, 129.38, 129.13, 127.14, 126.01, 120.25, 117.17, 113.43, 17.62, 15.48. HRMS (ESI+) Calculated $[M+H]^+$ 380.1255, observed 380.1261.

***Compound 4** – prepared according to a reported method with different starting reagents*[3]

The amidrazone **3** (250mg, 0.66mmol, 1eq) was dissolved in dry DCM (10mL). DBU (107mg, 0.69mmol, 1.05eq) and 5% Pd/C (22.4mg, 1.6% mol eq) were added and the solution was stirred in air at room temperature for 6h. The solution was filtered through a celite bed and the solvent was removed to obtain the crude product, which was purified by column chromatography (silica gel, 10% ethyl acetate in hexanes) to yield the radical product as a dark brown solid (135mg, 54%). HRMS (ASAP+) Calculated $[M+H]^+$ 377.1029, observed 380.1261. The EPR and UV spectra are presented in the main text (Figure 1b) and Figure S14 respectively.

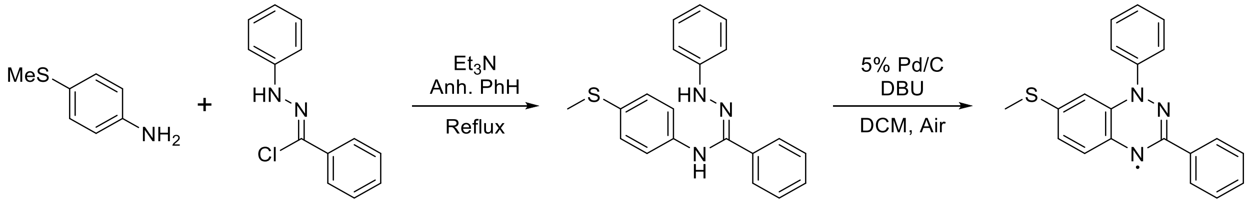

5 **6** **7**

Scheme S2. Synthesis of the Blatter radical derivative with only one thiomethyl linker, used in section 11.

The hydrazonyl chloride **5** was prepared according to literature methods.[2]

***Compound 6** – prepared according to a reported method with different starting reagents*[3]

The hydrazonyl chloride **5** (1.48g, 6.42mmol, 1eq) and 4-(methylthio)aniline (0.94g, 6.74mmol, 1.05eq) were dissolved in dry benzene (15mL) under an inert atmosphere. Triethylamine (0.97g, 9.62mmol, 1.5eq) was added, and the solution was refluxed for 4h. The reaction was quenched with cold water and diluted with ethyl acetate. The organic extracts were washed with water and brine and dried over $MgSO_4$. After removing the solvent, the crude product was purified by column chromatography (silica gel, 10-20% ethyl acetate in hexanes) to yield the amidrazone as a low melting point yellow solid (0.50g, 23%). ^{1}H-NMR (500 MHz, DMSO-d_6) δ 9.16 (s, 1H), 8.09 (s, 1H), 7.61 – 7.57 (m, 2H), 7.38 – 7.28 (m, 3H), 7.23 – 7.14 (m, 4H), 7.10 (d, J = 8.7, 2H), 6.73 (tt, J = 7.0, 1.4 Hz, 1H), 6.58 (d, J = 8.7, 2H), 2.36 (s, 3H). ^{13}C-NMR (500 MHz, DMSO-d_6) δ 145.76, 141.17, 136.97, 135.04, 128.92, 128.71, 128.26, 128.17, 126.68, 126.51, 118.57, 117.18, 112.63, 16.69. HRMS (ESI+) Calculated $[M+H]^+$ 334.1378, observed 334.1370.

***Compound 7** – prepared according to a reported method with different starting reagents*[3]

The amidrazone **6** (410mg, 1.23mmol, 1eq) was dissolved in dry DCM (8mL). DBU (190mg, 1.23mmol, 1eq) and 5% Pd/C (42mg, 1.6% mol eq) were added and the solution was stirred in air at room temperature for 6h. The solution was filtered through a celite bed and the solvent was removed to obtain the crude product, which was purified by column chromatography (silica gel, 15% ethyl acetate in hexanes) to yield the radical product as a dark brown solid (203mg, 50%). HRMS (ASAP+) Calculated $[M+H]^+$ 331.1143, observed 331.1147. The EPR is shown in Figure S10 below.

3. STM and STS experimental details

The Au(111) surface was prepared by repeated cycles of Ne^+ sputtering (1.5 keV) and annealing to 830 K. Low-temperature experiments were carried out with a home-built combined scanning tunneling/atomic force microscope, in ultrahigh vacuum ($p \approx 5\times10^{-11}$ mbar) and at a temperature of 6.1 K. Bias voltages are given as sample bias with respect to the tip. A sub-monolayer coverage of molecules was deposited onto the sample kept at ≅ 7 K inside the microscope. A mild Gaussian filtering has been applied to the STM images, in order to remove high frequency noise components. STS data (dI/dV) were acquired using lock-in detection of the tunnel current I by adding a 1.5 mV_{pp} modulation at 185 Hz to the sample bias voltage V.

4. X-ray measurement details and sample preparation

The X-ray spectroscopic measurements (XPS and NEXAFS) were all performed at the ALOISA beamline at the Elettra Synchrotron in Trieste. The radical films were prepared by evaporating the molecule from a crucible heated to ~170°C in a preparation chamber at a pressure of 10^{-7} to 10^{-8} mbar with a base pressure in the 10^{-10} mbar range. The deposition times varied between 30 to 180 s to obtain different film coverages. The measurement chamber was kept under ultrahigh-vacuum at a pressure lower than 10^{-10} mbar with the sample at ambient temperature.

The clean Au(111) surface was prepared by cycles of Ar^+ sputtering (1.5 keV) and annealing up to ~750 K. After each cleaning cycle, the surface was checked for cleanness by XPS in the carbon, nitrogen, oxygen and sulfur regions. The photoemission signal was detected by a hemispherical electron analyzer in normal emission geometry, with grazing (4°) photon beam incidence angle. The overall energy resolution was about 200 meV for the core-level XPS taken at a nominal photon energy of 515 eV and about 100 meV for the valence-band measurements taken at a nominal photon energy of 140 eV. The binding energy of the spectra was calibrated to the Au $4f_{7/2}$ peak at 84.0 eV or the Fermi edge at 0 eV.

5. Core-level XPS measurements

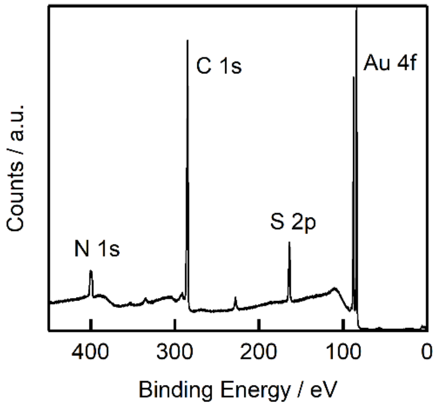

Figure S1. Wide energy range XPS scan of the multilayer of the Blatter radical derivative deposited on Au(111).

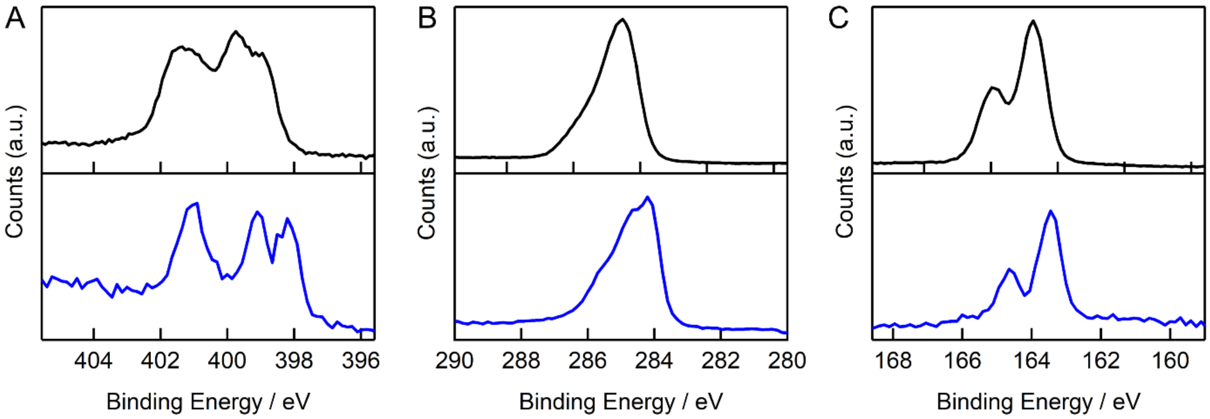

Figure S2. XPS of the (a) nitrogen 1s, (b) carbon 1s, and (c) sulfur 2p regions for the multilayer (black) and monolayer (blue) films. The 3 distinct nitrogen peaks are due to different chemical environments around the N atoms as detailed in the main text, and the sulfur peak shows a single 1:2 spin-orbit split doublet corresponding to only one sulfur environment.

6. DFT calculation of N 1s XPS spectrum

The geometry optimization of the isolated molecule was performed using DFT calculations with Gaussian09.[4] The B3LYP functional and 6-31G** basis set were used. The optimized geometry then served as input to GPAW, a DFT Python code based on the projector-augmented wave (PAW) method to calculate the N1s core electron binding energies (CEBEs) as well as the N 1s (K-edge) X-ray absorption spectra (section 8).[5-7]

We calculated the N 1s CEBEs of all three inequivalent nitrogen sites for the neutral radical with the PBE functional with a cell size of 25.6 Å and grid spacing of 0.2 Å using the delta Kohn-Sham scheme. The full core-hole PAW setups were created with GPAW and default parameter values. All calculations were spin-polarized due to the open-shell nature of the radical. Figure S3 shows the comparison of the calculated CEBEs and the experimental N 1s XPS spectrum of the multilayer film fit with 3 main peaks for the pristine molecule and a doublet for the damaged species present in the film (see section 7 for details). The calculated CEBEs were rigidly shifted to match the position of the lowest BE peak. The calculated core-level shifts match nicely with the fits of the three main peaks, which allows us to confirm the peak assignments from highest to lowest binding energy as N1, N2, and N4 as shown in Figure S3b.

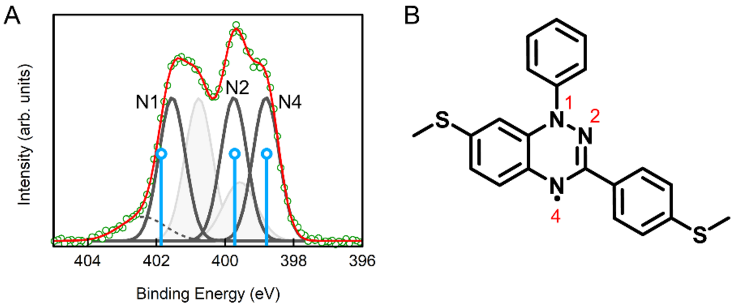

Figure S3. (a) Neutral radical multilayer N 1s XPS data (green circles) is shown fitted with three main peaks (dark gray traces) and an additional 2:1 doublet (light shaded gray). The blue sticks correspond to the DFT calculated core electron binding energies (CEBEs) of the three inequivalent nitrogen sites, which show good agreement with the experimental data. (b) Structure of the Blatter radical derivative with the corresponding nitrogen atoms labelled.

7. XPS beam damage

Here, we comment on the secondary doublet that appears in the N 1s region the multilayer film that was ascribed to a damaged radical species in the main text. In Figure S4, we show 3 other N 1s XPS spectra that arise from different exposure times to the X-ray irradiation due to successive scans on the same spot. This series of spectra can be fit with the same set of peaks arising from the pristine (black traces) and damaged (light gray) molecules. With increasing exposure time, it can be seen that the intensity of the signals from the pristine molecules decreases, while the signal intensity from the damaged molecules increases. We did not attempt to further characterize the damaged molecules.

Beam damage to the radical films was also noted by Ciccullo et al.,[8] which resulted in a secondary feature in the same ~400.5 eV region that we show here. However, the damage they reported was much less than what we observed. This is probably due to the higher photon flux of the synchrotron radiation we used, and also the different energy of incident beam used. In our measurement, the incident beam of 515 eV is closer to the resonance of nitrogen, which would produce more secondary electrons that can damage the film. Since we were aware of the beam damage from the outset of the experiments, we ensured that all spectra presented in this work were measured on pristine spots of the films.

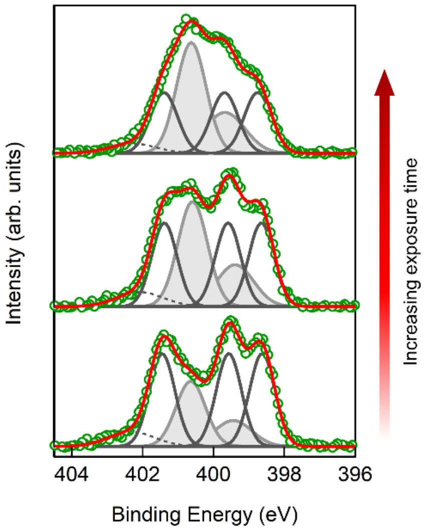

Figure S4. Evolution of the nitrogen 1s XPS spectrum with increasing exposure time on the same spot.

8. DFT calculation of N 1s NEXAFS spectra

Here, we calculate the N 1s (K-edge) absorption spectrum for the neutral Blatter radical. The X-ray absorption spectra were simulated for each inequivalent nitrogen atom separately using the half core-hole transition potential method as implemented in GPAW. The calculation parameters were the same as for the CEBE calculations described in section 6. We determine the absolute energy scale with a Delta Kohn-Sham calculation where we compute the total energy difference between the ground state and the first core excited state (in which an electron is removed from the core and placed in the LUMO) for each inequivalent nitrogen atom in the molecule. Finally, we offset the corresponding half-core-hole (transition potential) Kohn-Sham unoccupied orbital energies in such a way that the energy of the LUMO matches the previous computed Delta Kohn-Sham energy. The NEXAFS spectra were then obtained by combining all transitions from the different initial states and convoluting with a gaussian with a full width half maximum of 0.6 eV. An additional rigid shift was employed to match the simulated NEXAFS spectrum with the experimental data for better comparison. The calculated data is in very good agreement with the experimental spectra of the multilayer and monolayer.

Figure S5a shows the experimental (multilayer) and calculated N 1s absorption spectrum for the radical. The colored bars arise from the transitions from the correspondingly colored nitrogen atoms in Figure S5b. The dark and light bars of the same color differentiate transitions from the α and β spins respectively. There are 3 transitions in the neutral radical that are core transitions from the 3 inequivalent nitrogen atoms to the singly unoccupied molecular orbital (SUMO). As mentioned in the main text, the transitions in the calculated NEXAFS agree with the XPS results because the atom with the lowest (highest) XPS binding energy N4 (N1) is responsible for the lowest (highest) energy absorption feature in the NEXAFS. There is also a feature at ~399.2 eV, which we assign to the N2 → LUMO transition. In contrast to the core → SUMO transitions which have contribution from the β spins (since the α orbital is occupied), the N2 → LUMO transition has contribution from both α and β spins. The N2 → LUMO and the N1 → SUMO transitions overlap to form the highest intensity X-ray absorption feature in this region.

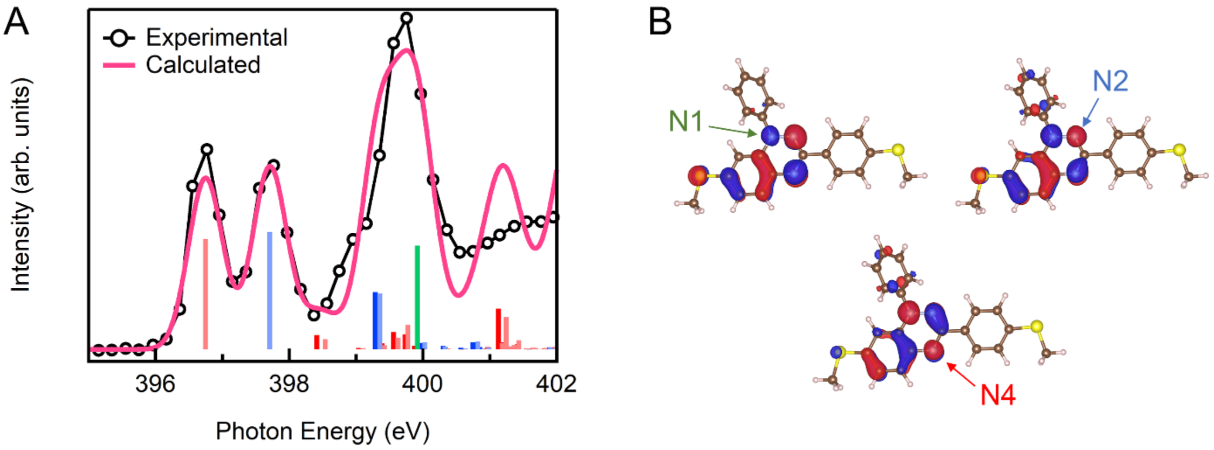

Figure S5. Calculated spin polarized half core-hole N 1s NEXAFS transitions. In (a), the experimental spectrum of the neutral radical (multilayer film, black trace) is compared to the calculated absorption spectrum (pink trace and colored bars) obtained from DFT transition potential calculations. Transitions from the individual N atoms indicated on the SUMOs in (b) are calculated and shown as the corresponding colored bars in (a). The dark and light bars of the same color indicate distinct transitions from the α and β spins respectively.

9. Polarization-dependent NEXAFS

Near edge X-ray absorption fine structure (NEXAFS) spectra were collected at a photon incident angle of 6° in partial electron yield by a wide acceptance angle channeltron. The polarization of the incident light was either parallel (*p-pol*) or perpendicular (*s-pol*) to the sample normal.

Polarization dependent nitrogen K-edge NEXAFS measurements show that the fused benzotriazinyl core of the molecules in the monolayer lie flat on the gold surface, with the π system perpendicular to the substrate. The 399.3 eV peak, which is a transition to the π^* LUMO (see DFT calculations in section 8 for assignment details), is strongest when the incident light is polarized perpendicular (*p-pol*) to the substrate but is suppressed when light is polarized parallel (*s-pol*) to the substrate (Figure S6a).[9,10] The carbon K-edge *p-pol* and *s-pol* NEXAFS spectra (Figure S6b) show a less pronounced dichroism of the main π* resonances at around 285 eV, most probably because the two pendant phenyl rings bound with a single bond to the fused benzotriazinyl core are able to rotate freely out of the perpendicular plane as portrayed in Figure 1c of the main text.

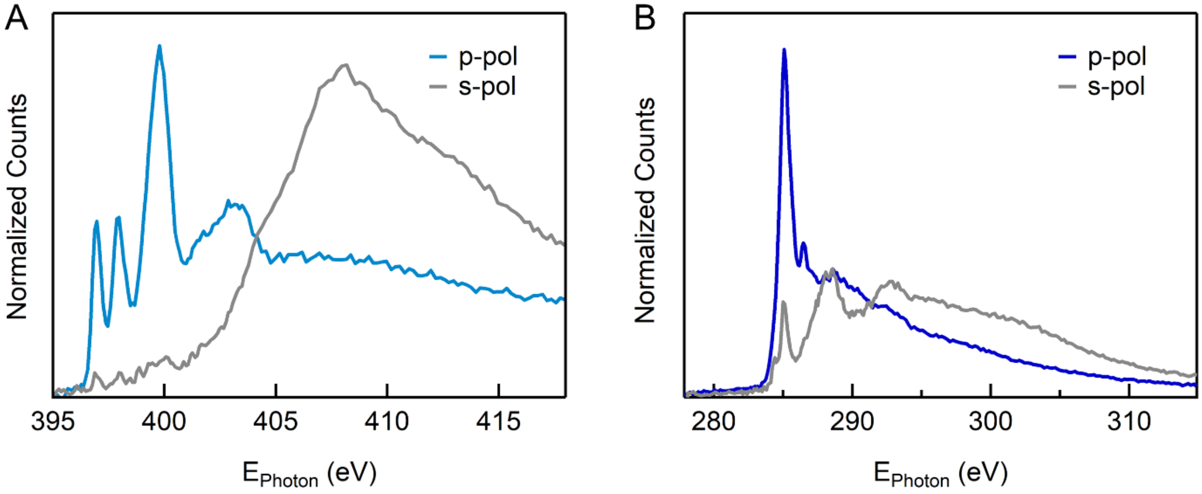

Figure S6. Nitrogen K-edge (a) and carbon K-edge (b) NEXAFS spectra of the Blatter radical derivative. Both p- and s-pol spectra are shown.

10. Gas-phase DFT calculations

The geometry optimization of the isolated molecule was performed using DFT calculations with Gaussian09.[4] The B3LYP functional and 6-31G** basis set were used. The calculated ground state molecular orbitals of the neutral and oxidized radical in the gas phase are shown in Figure S7. They are very similar to the orbitals calculated for the Blatter without any thiomethyl groups.[11] Note that for the neutral radical, unrestricted DFT calculates the spin α and spin β orbitals separately. The SOMO (α) and SUMO (β) pair are identical since they are essentially the same orbital. The orbitals above and below these are paired up as well.

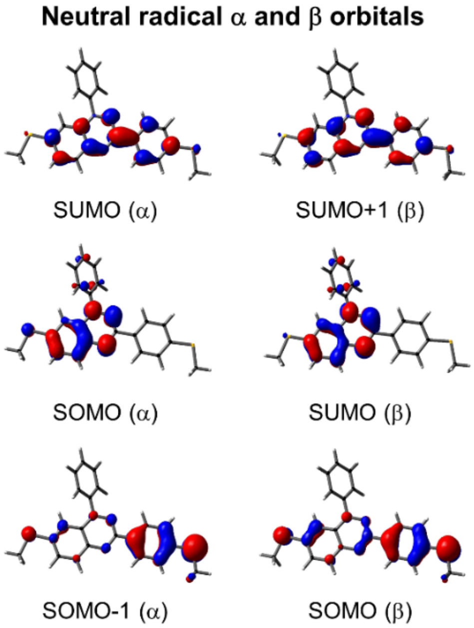

Figure S7. Orbitals of the neutral Blatter derivative visualized with an isovalue of 0.04.

11. Single molecule conductance measurements and measurement of oxidized radical

Conductance measurements were performed using a home-built modified Scanning Tunneling Microscope (STM). We used 0.25 mm diameter cut gold wire (99.95%, Alfa Aesar) as the STM tips and 100 nm gold-coated (99.999%, Alfa Aesar) steel pucks as substrates. A commercially available single-axis piezoelectric positioner (Nano-P-15, Mad City Labs) was used to achieve sub-angstrom level control of the tip-substrate distance. The setup was controlled using a custom program written in IgorPro. Measurements were performed in ambient conditions at room temperature. All gold substrates were cleaned with a UV / ozone cleaning lamp for 20 min before use. 1000 conductance traces were collected on each pristine substrate to check for contaminants prior to adding the solutions of molecules that were measured. For the measurement of the neutral radical shown in figure 4a of the main text, several drops of a 0.1 mM solution of the radical in trichlorobenzene were added to the substrate and the measurements were performed as described in the main text. The current and voltage data were acquired at 40 kHz.

To obtain the conductance trace of the oxidized the radical shown in figure 4a of the main text, we used tris(4-bromophenyl)ammoniumyl hexachloroantimonate (BAHA) to chemically generate the oxidized species. A 0.4 mM solution of the Blatter radical derivative with 1 equivalent of BAHA in dry dichloromethane was prepared. The solution was stirred for 10 min at room temperature and diluted to 0.1 mM with trichlorobenzene. This solution of 0.1 mM cation in 1:3 dichloromethane to trichlorobenzene mixture was then dropped directly onto the gold substrate in the STM setup, and break junction measurements were performed.

12. Conductance noise measurements

We characterized the conductance noise of the molecular junctions to differentiate between through-bond and through-space charge transport using the method described by Adak et al.[12] In order to measure the noise, we modify the STM-BJ measurement technique as follows. We first form a contact between the tip and substrate in an environment of the molecules and then break the contact by withdrawing the tip from the substrate at a speed of 20 nm/s. After a fixed elongation of 2.3 nm, we hold the junction for 150 ms and record the conductance with a 100 kHz sampling rate applying a bias voltage of 200 mV. We select traces that sustain a molecular junction during the hold period and calculate the discrete Fourier transform of this data. Out of a total of 71,000 traces measured using this modified ramp, 1749 sustained a high-conducting junction during the 150 ms hold period (Figure S8b) while 2378 sustained a low conducting junction (Figure S8c). These traces were selected for analysis. Two quantities are calculated from the measured conductance while the junction is held for each of these traces: the average conductance (G) and the normalized noise power (power spectrum density (PSD)/G). The PSD is obtained from the square of the integral of the discrete Fourier transform of the measured conductance between 100 Hz to 1000 Hz. The lower frequency limit is constrained by the mechanical stability of the setup. The upper limit is determined by the input noise of the current amplifier. Using these quantities, we create 2D histograms of the normalized noise power against the average conductance. The relation between noise power and conductance is extracted by determining the exponent n for which PSD/G and G are not correlated. We have previously shown that the relationship between flicker noise power (PSD) and junction conductance (G) follows a power law dependence (PSD ~ G^n) with the scaling exponent (n) being indicative of the electronic coupling type: n=1 is characteristic of through-bond coupling while n=2 is characteristic for through-space coupled junctions. Details of these derivations are presented in Adak et al.[12]

From our data, we find that the high-conductance junctions have an exponent n=1.1 (Figure S8e). This indicates that the thiomethyl-terminated molecular junctions are coupled through an Au-S bond, as depicted on top in Figure S8d. In contrast, the data in Figure S8f for the low conducting junctions have an exponent n=1.8. This indicates that conductance involves through-space transport as detailed further in the work of Magyarkuti et al., and as depicted on the bottom of Figure S8d.[13]

As a second control, we also synthesized a derivative of the Blatter radical that has only one gold-binding thiomethyl linker; this molecule shows a single conductance peak (Figure S9a), demonstrating the strong propensity for this family of radicals to form dimer junctions. The synthesis of this molecule is reported in section 2 and the EPR spectrum is shown in Figure S10. We find that propensity for the Blatter radicals to form these dimer junctions is so strong that lowering the concentration by a factor of 1000 does not lower the probability of their formation (Figure S9b). At the lowest concentration we observed the monomer peak (1 μM), we also observed the dimer peak. From previous investigations of dimer junctions, lower concentration was found to lower the probability of dimer formation.[13]

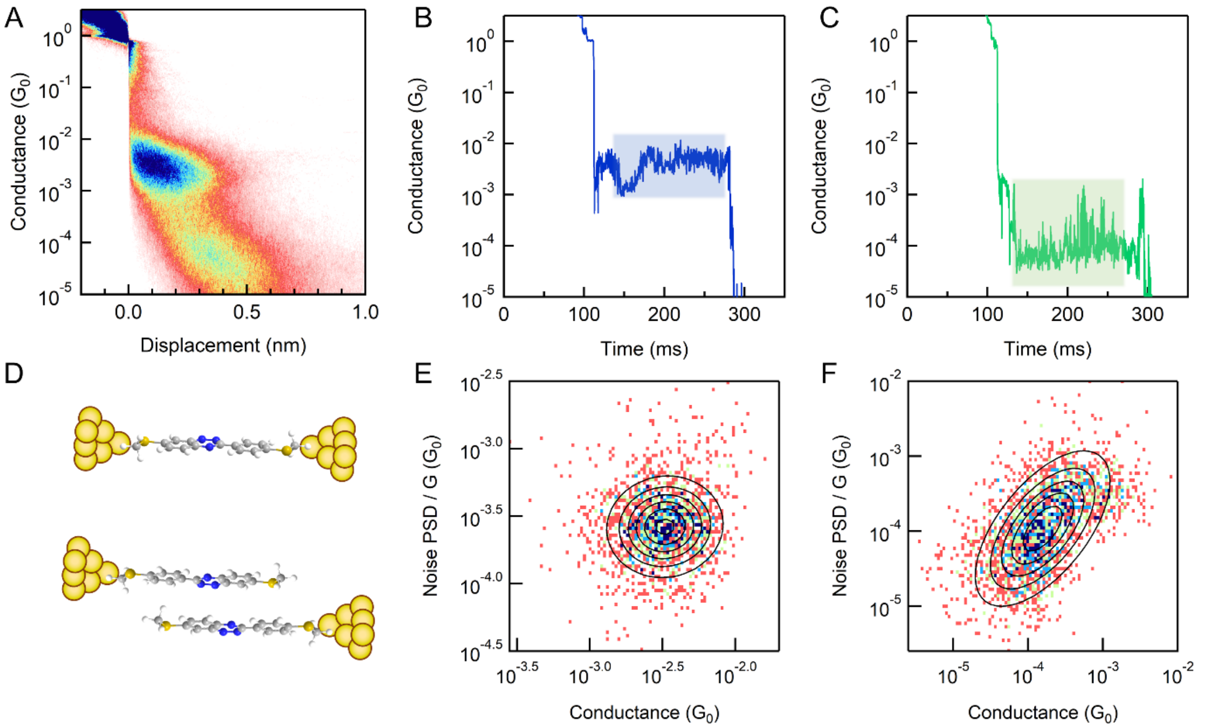

Figure S8. (a) 2D conductance histogram of the Blatter radical derivative. Individual traces from the fixed-hold experiments for (b) the high conductance and (c) low conductance peaks. (d) Representation of the monomer and dimer junctions formed. Normalized noise power versus conductance histograms for the (e) high conductance and (f) low conductance peaks. See text for details.

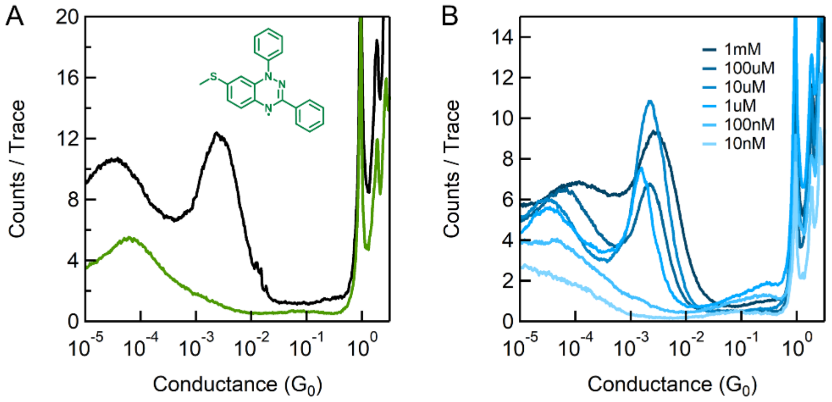

Figure S9. (a) Conductance histogram of the Blatter radical derivative with two thiomethyl linkers (black trace, see Figure S11b for structure), along with the histogram of the radical with only one thiomethyl linker (green). The structure of the radical with only one linker is shown inset. (b) Conductance histograms of the Blatter radical derivative (with two thiomethyl linkers) at varying concentrations. At concentrations below 1 μM, no conductance peaks are visible.

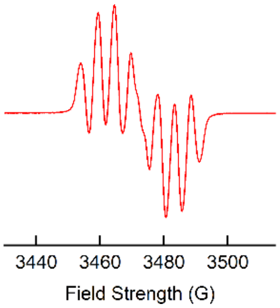

Figure S10. EPR spectrum of Blatter radical 7 in toluene solution. The structure is shown in the inset of Figure S9a.

13. 4,4’-di(methylthio)stilbene conductance measurement

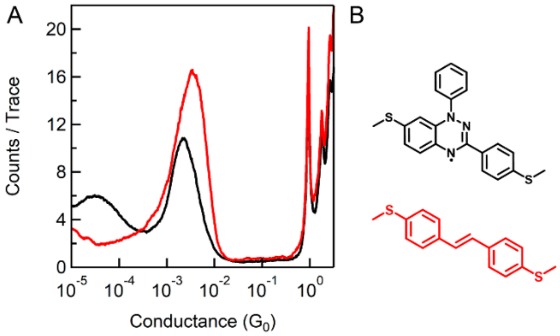

Figure S11. (a) Conductance histogram of the Blatter radical derivative (black trace) compared to 4,4’-di(methylthio)stilbene (red trace). The measurements were performed in trichlorobenzene at a concentration of 10μM and an applied bias of 100mV. The main conductance peaks coincide, indicating that the radical has been converted into a closed shell species. The stilbene shows no low conductance peak. (b) Structure of the Blatter radical derivative and 4,4’-di(methylthio)stilbene in the colors corresponding to the traces in (a).

14. In-situ cyclic voltammetry with gold electrodes

To check the redox stability of the Blatter radical in the gold junction, we perform cyclic voltammetry in the STM-BJ setup. For these measurements, we used a tip coated with Apiezon wax to ensure a small tip area to reduce background capacitive current.[14] A 1 mM solution of the Blatter radical derivative in anhydrous propylene carbonate with 0.1 M tetrabutylammonium perchlorate (TBAP) as supporting electrolyte was prepared. The radical solution was dropped onto the gold substrate, and 1000 conductance traces were obtained to ensure that the molecule is indeed present. Then, the tip is retracted to ~1 μm above the substrate, and the cyclic voltammetry sweep is performed, i.e. the current at the tip is monitored as the voltage applied to the tip is swept.

Since there is no reference electrode, we referenced the results to the ferrocene oxidation wave. Figure S12 shows the cyclic voltammetry sweep of the Blatter radical derivative in blue. The orange trace shows a solution of 1 mM radical with 0.5 mM ferrocene and 0.1 M TBAP in solution. Clearly, the radical is more easily oxidized than ferrocene by ~0.2 V, which agrees with the bulk cyclic voltammetry measurement on platinum disk described below. Additionally, the oxidation wave of the radical occurs at a very small bias in our setup, providing further evidence that the molecule is also oxidized once a bias is applied to measure the molecular conductance.

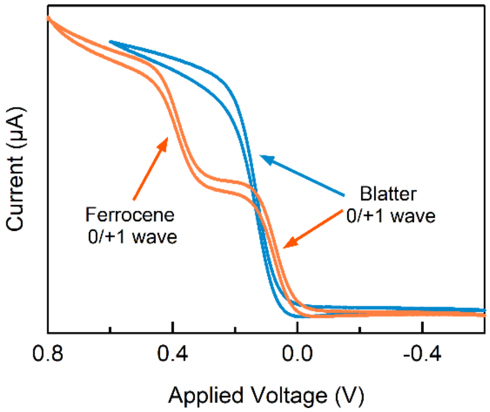

Figure S12. In-situ cyclic voltammogram of the Blatter radical derivative (blue) and of both the radical and ferrocene (orange) in anhydrous propylene carbonate. The potential is calibrated to the onset of the Fc/Fc+ oxidation wave.

15. Platinum electrode cyclic voltammetry

Cyclic voltammetry was performed using single cell setup with a CH Instruments Electrochemical Analyser Potentiostat. The set up consists of: a) platinum working electrode, b) platinum wire counter electrode, and c) Ag/AgCl reference electrode, all purchased from BASi. Figure S13 shows the cyclic voltammogram of the Blatter radical derivative. The measurement was carried out in dichloromethane solution containing 0.1 M of supporting electrolyte, tetrabutylammoniumhexafluorophosphate (TBAPF$_6$), with ~1 mg/mL of the desired compound. A scan rate of 0.1 Vs^{-1} was used. Both redox processes are reversible over several cycles.

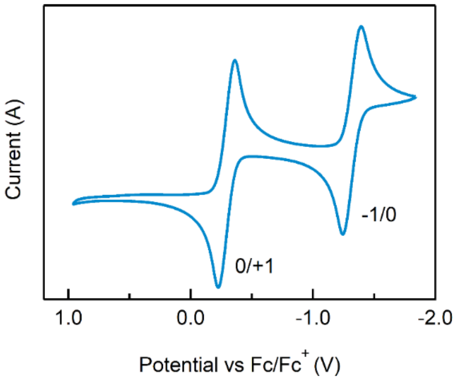

Figure S13. Cyclic voltammogram of the Blatter radical derivative calibrated to the $E_{1/2}^{Ox}$ *of ferrocene, which is set at 0 V. The oxidation and reduction potentials of the radical are* $E_{1/2}^{Ox}$ = -0.29 V *and* $E_{1/2}^{Red}$ = -1.32 V. *This corresponds to a SOMO and SUMO energy of -4.51 and -3.48 eV respectively.*

16. Chemical oxidation study – UV-Vis and NMR

To chemically oxidize the Blatter radical derivative, we use 1 electron oxidants with sufficient oxidation potential. Tris(4-bromophenyl)ammoniumyl hexachloroantimonate (BAHA) has an oxidation potential of 0.70 V vs ferrocene, while silver hexafluoroantimonate (AgSbF$_6$) has an oxidation of 0.65 V vs ferrocene.[15]

For the UV titration, a 10 µM solution of the Blatter radical derivative in dichloromethane (3 mL) was placed in a UV cuvette. A 100 µM solution of BAHA oxidant was added in 50 µL aliquots. Therefore, an addition of 6 aliquots results in a 1:1 ratio of radical to oxidant, leading to full conversion of the radical into its cation. Figure S14 shows the resulting UV-Vis spectra after addition of up to 2 equivalents of BAHA. The black and purple traces in both graphs are the neutral radical and closed shell cation respectively. In Figure S14b, it can be seen that the addition of BAHA beyond 1 equivalent only increases the peak heights in regions where BAHA absorbs. The UV-Vis spectrum of BAHA is shown in blue for reference. Therefore, there is no further oxidation occurring.

For the NMR oxidation, a 3 mM solution of the Blatter derivative with 1 equivalent of $AgSbF_6$ in deuterated dichloromethane was prepared. The peaks are reported as follows: ^{1}H-NMR (400 MHz, CD_2Cl_2) δ 8.44 (d, *J* = 8.8 Hz, 2H), 8.28 (d, *J* = 9.2 Hz, 1H), 8.13 (dd, *J* = 9.6, 2.0 Hz, 1H), 7.94 – 7.81 (m, 5H), 7.45 (d, *J* = 8.8 Hz, 2H), 7.35 (d, *J* =2.0 Hz, 1H), 2.60 (s, 3H), 3.58 (s, 3H). The NMR spectrum is shown in Figure S15.

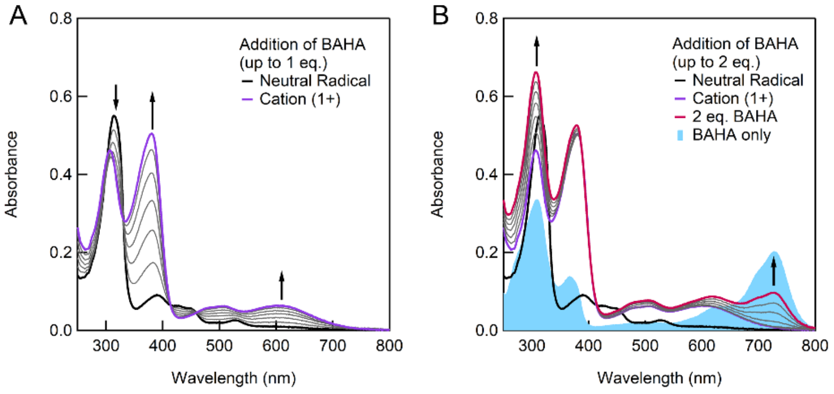

Figure S14. (a) Evolution of UV-Vis spectrum of the Blatter radical derivative as 1 equivalent of BAHA is added in six steps. The spectrum of the neutral radical is the bold black trace, with the cation in purple. (b) Evolution of the UV-Vis spectrum as 1 additional equivalent of BAHA is added in six steps. The end point is shown in red. The shaded light blue graph is the spectrum of the BAHA oxidant.

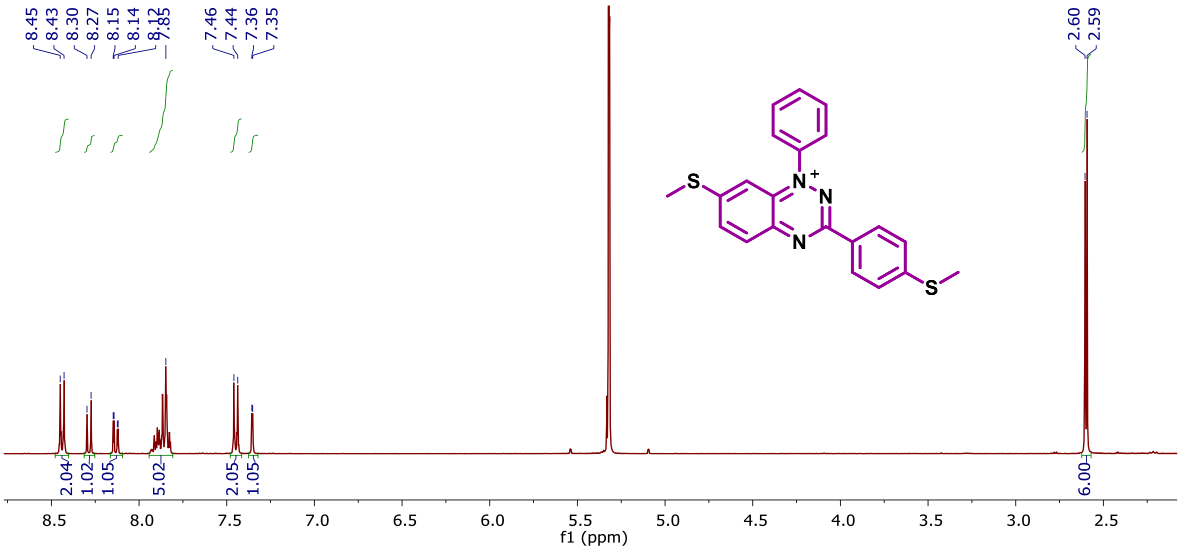

Figure S15. NMR spectrum of the oxidized Blatter radical derivative.

17. Optimized coordinates for gas phase DFT calculations

Table S1. Optimized DFT coordinates calculated for the neutral Blatter radical.

Center Number	Element	Coordinates (angstroms)			Center Number	Element	Coordinates (angstroms)		
		X	Y	Z			X	Y	Z
1	C	-3.842082	-1.645845	-0.055901	23	S	-5.614615	-1.610149	-0.228363
2	C	-3.088226	-2.821407	0.117179	24	C	-6.071817	-3.369878	-0.352785
3	C	-1.707704	-2.750194	0.225738	25	S	6.978972	0.036893	-0.089750
4	C	-1.028295	-1.518319	0.187647	26	C	7.586046	-1.679264	-0.016575
5	C	-1.808494	-0.329896	0.064402	27	H	-3.572630	-3.789496	0.156644
6	C	-3.196154	-0.403518	-0.088256	28	H	-1.107039	-3.647269	0.332136
7	N	0.336771	-1.489615	0.237451	29	H	-3.775193	0.498574	-0.242789
8	C	0.905742	-0.284373	0.103747	30	H	2.618903	-2.347988	0.147887
9	N	0.276076	0.892999	0.013108	31	H	5.080523	-2.301332	0.070690
10	N	-1.088367	0.867030	0.067380	32	H	4.964069	2.005589	-0.104971
11	C	2.387732	-0.220216	0.062089	33	H	2.498894	1.927746	-0.025634
12	C	-1.694160	2.161640	0.050608	34	H	-3.014670	1.763542	1.708473
13	C	3.141151	-1.399875	0.090970	35	H	-4.024265	4.024664	1.673850
14	C	4.533266	-1.366158	0.047653	36	H	-3.246435	5.714870	0.023535
15	C	5.207795	-0.140566	-0.025500	37	H	-1.446523	5.125031	-1.588292
16	C	4.455570	1.046975	-0.052200	38	H	-0.447852	2.845048	-1.557626
17	C	3.069446	1.006418	-0.008913	39	H	-7.150166	-3.378621	-0.523403
18	C	-2.693176	2.492936	0.973353	40	H	-5.857770	-3.910427	0.571752
19	C	-3.251853	3.770294	0.954492	41	H	-5.574728	-3.851347	-1.197675
20	C	-2.810393	4.720736	0.032669	42	H	8.674889	-1.606882	-0.051548
21	C	-1.799045	4.389319	-0.871741	43	H	7.242683	-2.263347	-0.873370
22	C	-1.238224	3.114432	-0.867104	44	H	7.293491	-2.168609	0.915158

18. NMR spectra

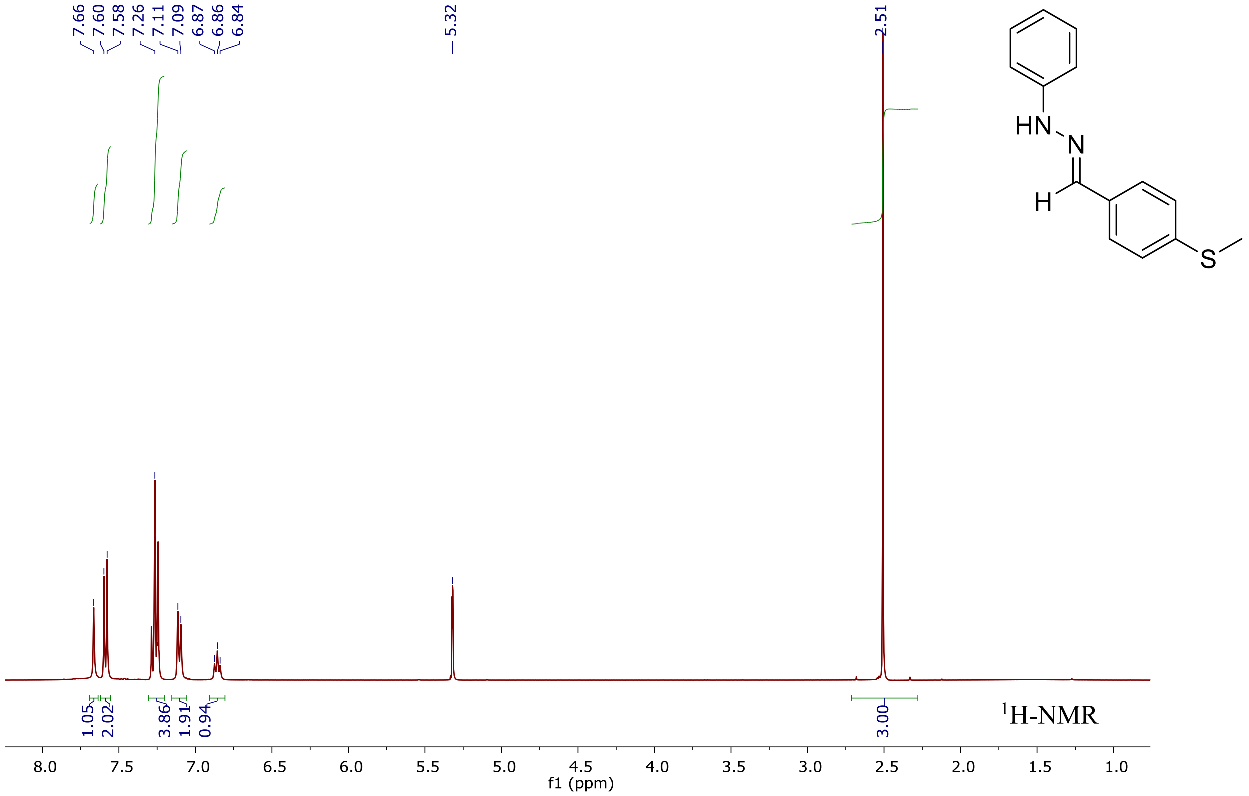

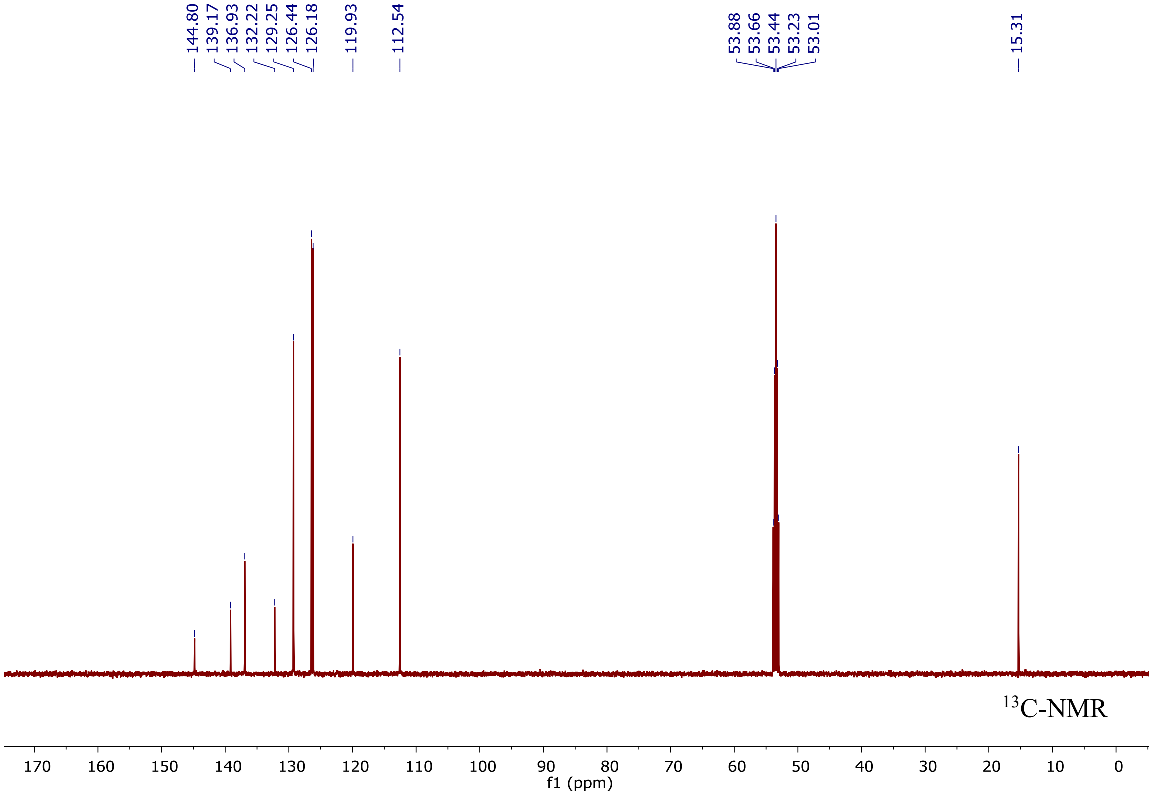

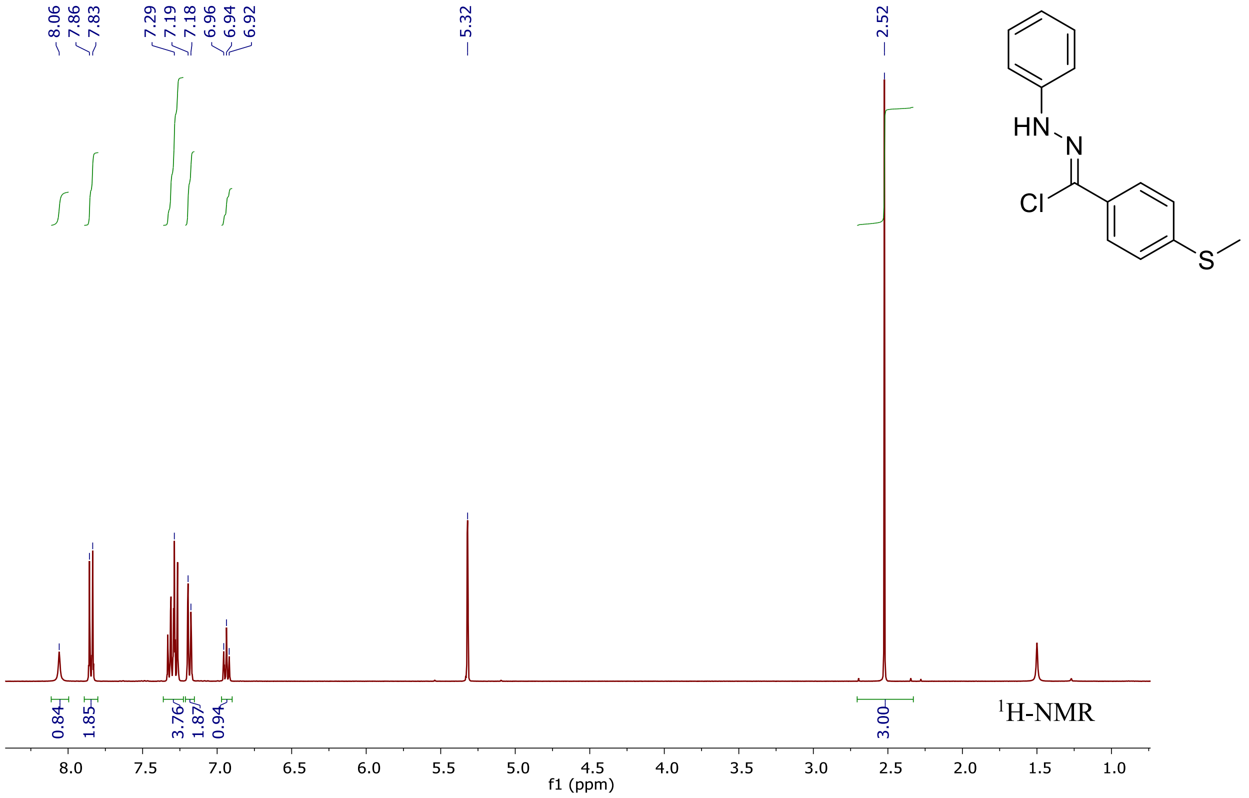
8.06
7.86
7.83
7.29
7.19
7.18
6.96
6.94
6.92
5.32
2.52
0.84
1.85
3.76
1.87
0.94
3.00
HN
N
Cl
S
^{1}H-NMR
8.0
7.5
7.0
6.5
6.0
5.5
5.0
4.5
4.0
3.5
3.0
2.5
2.0
1.5
1.0
f1 (ppm)

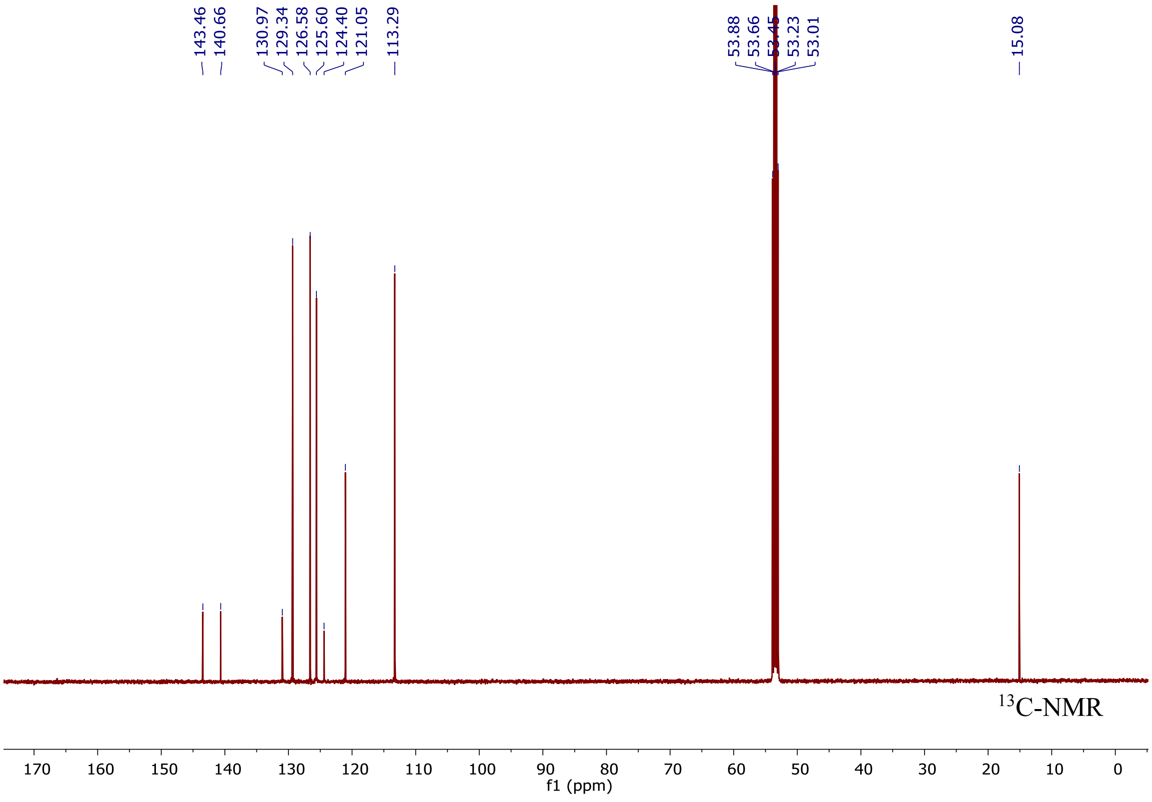
143.46
140.66
130.97
129.34
126.58
125.60
124.40
121.05
113.29
53.88
53.66
53.45
53.23
53.01
15.08
^{13}C-NMR
170
160
150
140
130
120
110
100
90
80
70
60
50
40
30
20
10
0
f1 (ppm)

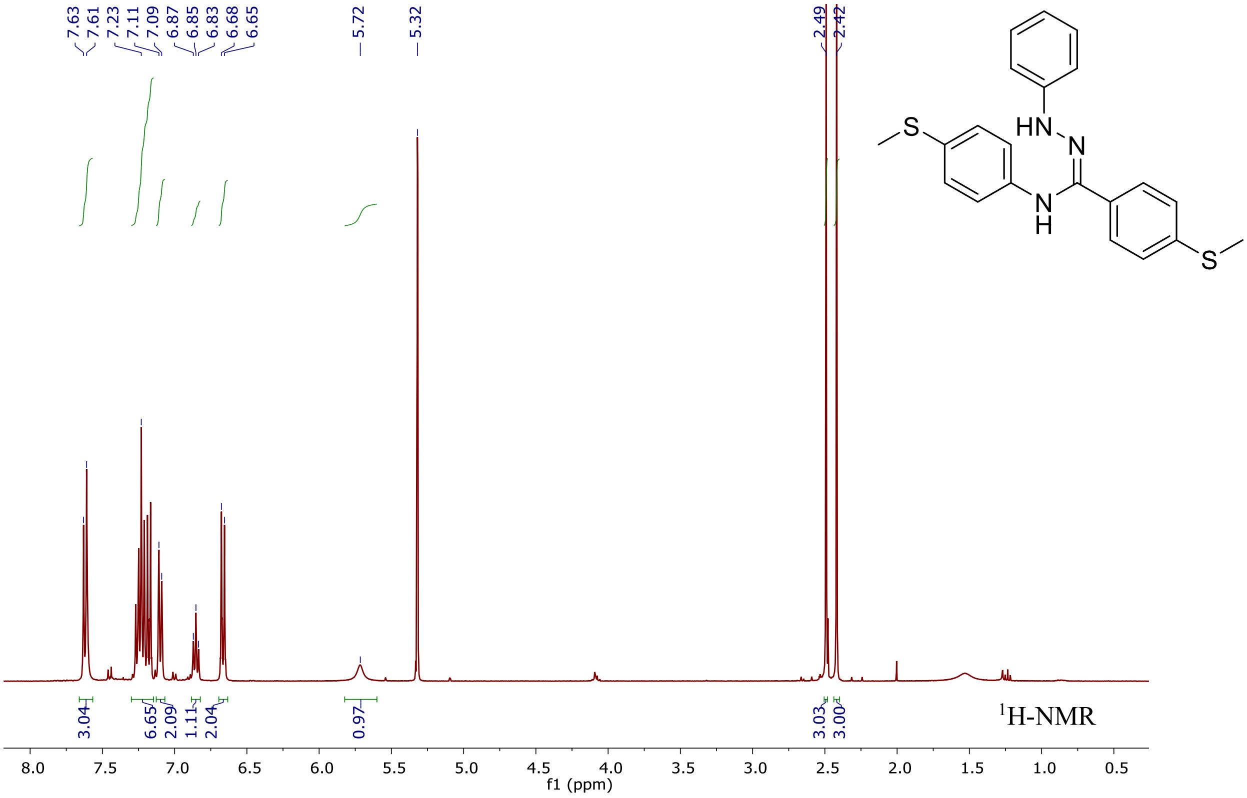
7.63
7.61
7.23
7.11
7.09
6.87
6.85
6.83
6.68
6.65
5.72
5.32
2.49
2.42
3.04
6.65
2.09
1.11
2.04
0.97
3.03
3.00
S
HN
N
N
H
S
^{1}H-NMR
8.0
7.5
7.0
6.5
6.0
5.5
5.0
4.5
4.0
3.5
3.0
2.5
2.0
1.5
1.0
0.5
f1 (ppm)

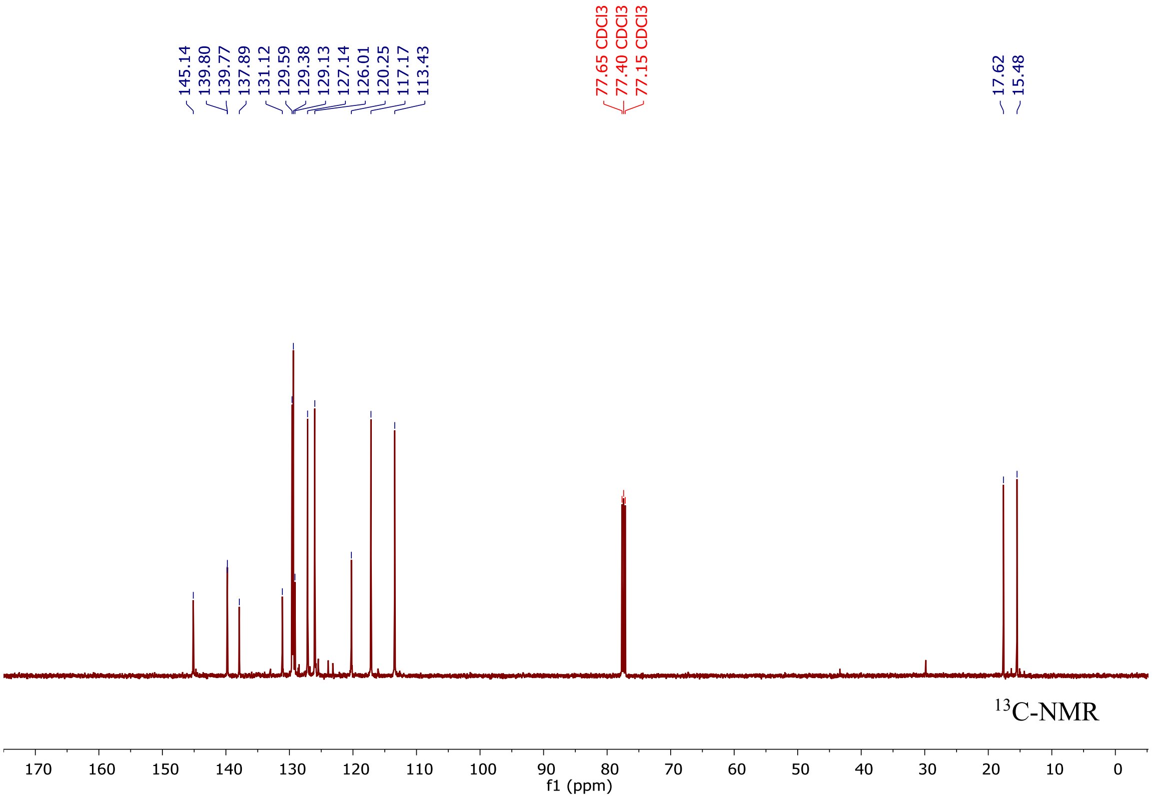
145.14
139.80
139.77
137.89
131.12
129.59
129.38
129.13
127.14
126.01
120.25
117.17
113.43
77.65 CDCl3
77.40 CDCl3
77.15 CDCl3
17.62
15.48
^{13}C-NMR
170
160
150
140
130
120
110
100
90
80
70
60
50
40
30
20
10
0
f1 (ppm)

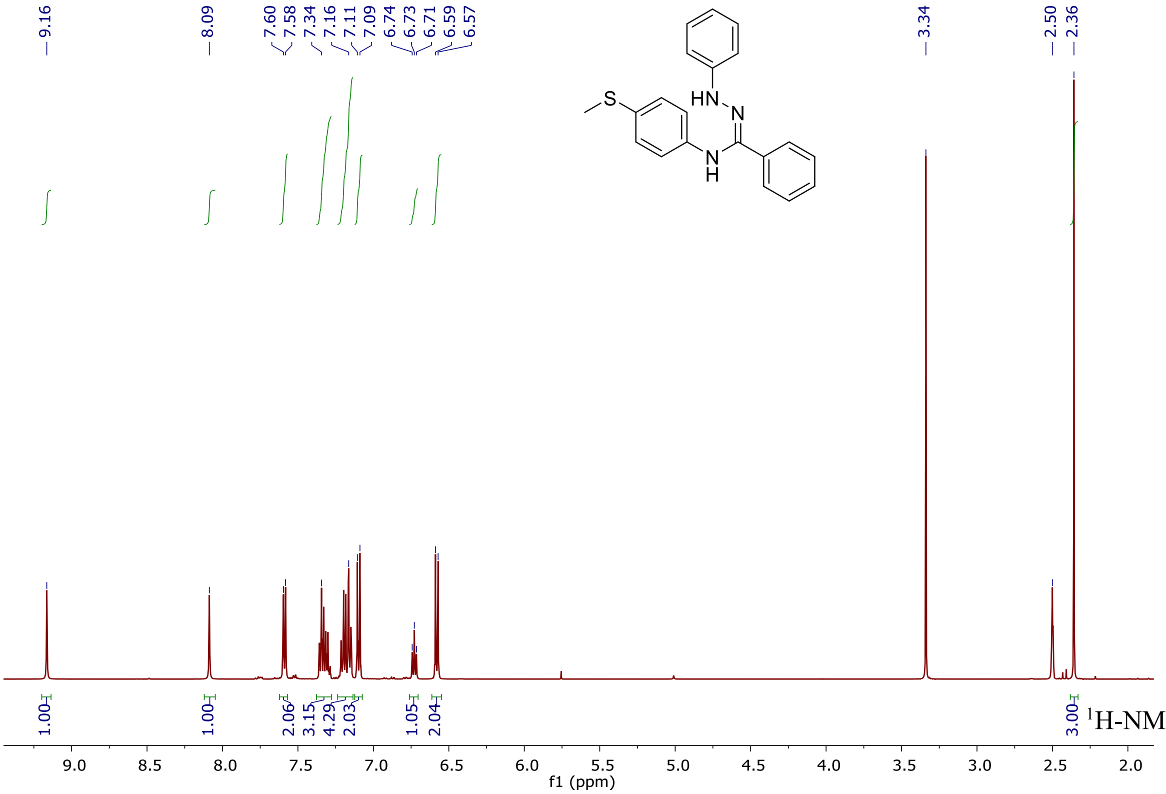

^{1}H-NMR

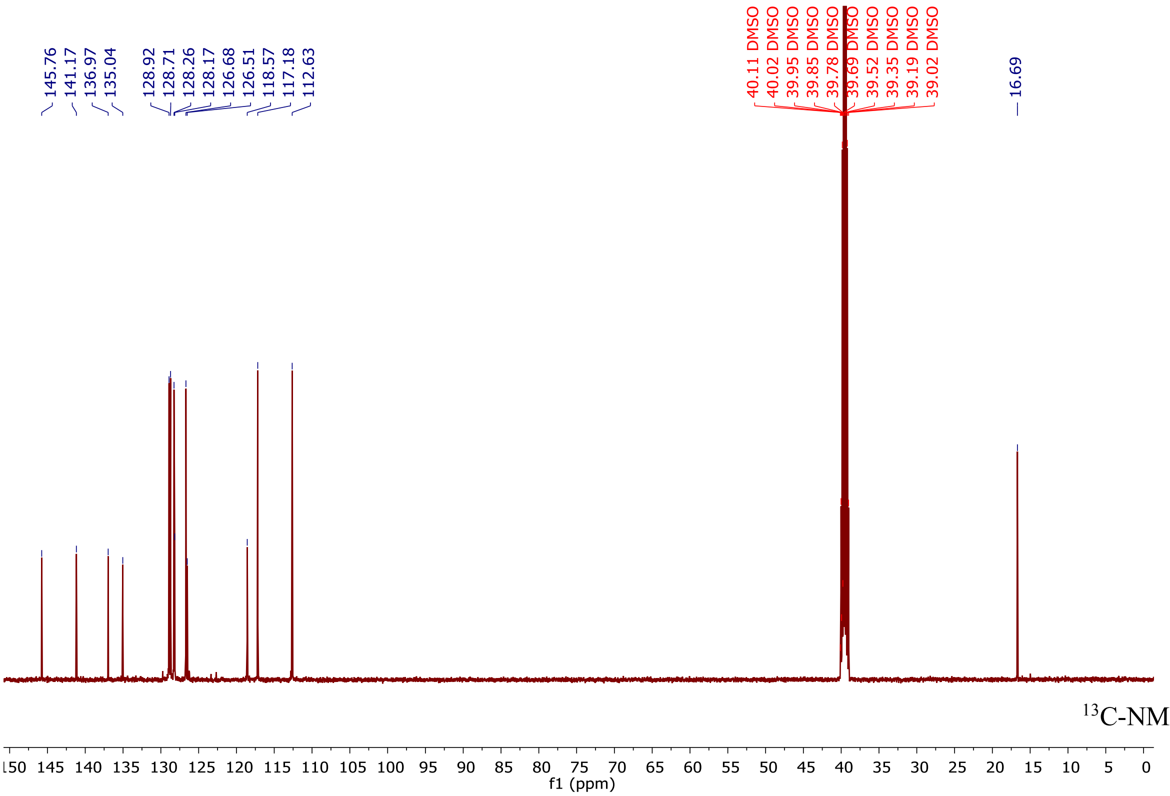

^{13}C-NMR

19. References

(1) Vantomme, G.; Jiang, S.; Lehn, J.-M. *J. Am. Chem. Soc.* **2014**, *136*, 9509-9518.

(2) Patel, H. V.; Vyas, K. A.; Pandey, S. P.; Fernandes, P. S. *Tetrahedron* **1996**, *52*, 661-668.

(3) Koutentis, P. A.; Lo Re, D. *Synthesis* **2010**, *12*, 2075-2079.

(4) Frisch, M. J.; Trucks, G. W.; Schlegel, H. B.; Scuseria, G. E.; Robb, M. A.; Cheeseman, J. R.; Scalmani, G.; Barone, V.; Mennucci, B.; Petersson, G. A.; Nakatsuji, H.; Caricato, M.; Li, X.; Hratchian, H. P.; Izmaylov, A. F.; Bloino, J.; Zheng, G.; Sonnenberg, J. L.; Hada, M.; Ehara, M.; Toyota, K.; Fukuda, R.; Hasegawa, J.; Ishida, M.; Nakajima, T.; Honda, Y.; Kitao, O.; Nakai, H.; Vreven, T.; Montgomery, J. A.; Peralta, J. E.; Ogliaro, F.; Bearpark, M.; Heyd, J. J.; Brothers, E.; Kudin, K. N.; Staroverov, V. N.; Kobayashi, R.; Normand, J.; Raghavachari, K.; Rendell, A.; Burant, J. C.; Iyengar, S. S.; Tomasi, J.; Cossi, M.; Rega, N.; Millam, J. M.; Klene, M.; Knox, J. E.; Cross, J. B.; Bakken, V.; Adamo, C.; Jaramillo, J.; Gomperts, R.; Stratmann, R. E.; Yazyev, O.; Austin, A. J.; Cammi, R.; Pomelli, C.; Ochterski, J. W.; Martin, R. L.; Morokuma, K.; Zakrzewski, V. G.; Voth, G. A.; Salvador, P.; Dannenberg, J. J.; Dapprich, S.; Daniels, A. D.; Farkas; Foresman, J. B.; Ortiz, J. V.; Cioslowski, J.; Fox, D. J. Gaussian 09, Revision D.01, Gaussian, Inc., Wallingford CT, 2009.

(5) Mortensen, J. J.; Hansen, L. B.; Jacobsen, K. W. *Phys. Rev. B* **2005**, *71*, 035109.

(6) Enkovaara, J.; Rostgaard, C.; Mortensen, J. J.; Chen, J.; Dułak, M.; Ferrighi, L.; Gavnholt, J.; Glinsvad, C.; Haikola, V.; Hansen, H. A.; Kristoffersen, H. H.; Kuisma, M.; Larsen, A. H.; Lehtovaara, L.; Ljungberg, M.; Lopez-Acevedo, O.; Moses, P. G.; Ojanen, J.; Olsen, T.; Petzold, V.; Romero, N. A.; Stausholm-Møller, J.; Strange, M.; Tritsaris, G. A.; Vanin, M.; Walter, M.; Hammer, B.; Häkkinen, H.; Madsen, G. K. H.; Nieminen, R. M.; Nørskov, J. K.; Puska, M.; Rantala, T. T.; Schiøtz, J.; Thygesen, K. S.; Jacobsen, K. W. *J. Phys.: Condens. Matter* **2010**, *22*, 253202.

(7) Bahn, S. R.; Jacobsen, K. W. *Comput. Sci. Eng.* **2002**, *4*, 56-66.

(8) Ciccullo, F.; Gallagher, N. M.; Geladari, O.; Chassé, T.; Rajca, A.; Casu, M. B. *ACS Appl. Mater. Interfaces* **2016**, *8*, 1805-1812.

(9) Batra, A.; Kladnik, G.; Vázquez, H.; Meisner, J. S.; Floreano, L.; Nuckolls, C.; Cvetko, D.; Morgante, A.; Venkataraman, L. *Nat. Commun.* **2012**, *3*, 1086.

(10) Adak, O.; Kladnik, G.; Bavdek, G.; Cossaro, A.; Morgante, A.; Cvetko, D.; Venkataraman, L. *Nano Lett.* **2015**, *15*, 8316-8321.

(11) Yan, B.; Cramen, J.; McDonald, R.; Frank, N. L. *Chem. Commun.* **2011**, *47*, 3201-3203.

(12) Adak, O.; Rosenthal, E.; Meisner, J.; Andrade, E. F.; Pasupathy, A. N.; Nuckolls, C.; Hybertsen, M. S.; Venkataraman, L. *Nano Lett.* **2015**, *15*, 4143-4149.

(13) Magyarkuti, A.; Adak, O.; Halbritter, A.; Venkataraman, L. *Nanoscale* **2018**, *10*, 3362-3368.

(14) Nagahara, L. A.; Thundat, T.; Lindsay, S. M. *Rev. Sci. Instrum.* **1989**, *60*, 3128-3130.

(15) Connelly, N. G.; Geiger, W. E. *Chem. Rev.* **1996**, *96*, 877-910.